Magnetic Resonance in Medicine 54:373–385 (2005)

Optimizing Brain Tissue Contrast with EPI: A Simulated Annealing Approach

Vasiliki N. Ikonomidou,* Peter van Gelderen, Jacco A. de Zwart, Masaki Fukunaga, and Jeff H. Duyn

A new magnetization preparation and image acquisition scheme was developed to obtain high-resolution brain images with optimal tissue contrast. The pulse sequence was derived from an optimization process using simulated annealing, without prior assumptions with regard to the number of radiofrequency (RF) pulses and flip angles. The resulting scheme combined two inversion pulses with the acquisition of three images with varying contrast. The combination of the three images allowed separation of gray matter (GM), white matter (WM), and cerebrospinal fluid (CSF) based on T_1, contrast. It also enabled the correction of small errors in the initial T_1 estimates in postprocessing. The use of three-dimensional (3D) sensitivity-encoded (SENSE) echo-planar imaging (EPI) for image acquisition made it possible to achieve a 1.15^3 mm^3 isotropic resolution within a scan time of 10 min 21 s. The cortical GM signal-to-noise ratio (SNR) in the calculated GM-only image varied between 30 and 100. The novel technique was evaluated in combination with blood oxygen level-dependent (BOLD) functional magnetic resonance imaging (fMRI) on human subjects, and provided for excellent coregistration of anatomical and functional data. Magn Reson Med 54:373–385, 2005. Published 2005 Wiley-Liss, Inc.†

Key words: brain tissue labeling; T_1 weighting; optimization (simulated annealing); functional mapping; double inversion recovery

The excellent soft-tissue contrast provided by MRI is one of the main advantages of this technique over X-ray CT, especially in imaging of the brain. It allows one to distinguish between different tissue types, as well as to obtain detailed anatomical maps of human cortical architecture.

Brain tissue can be classified into three broad categories: white matter (WM), gray matter (GM), and cerebrospinal fluid (CSF). Their relative volume and precise location convey potentially important information for the diagnosis and treatment of disease, as well as for the general understanding of brain anatomy and function (1). Tissue characterization relies heavily on high-contrast MR images, which can be obtained by techniques such as T_1-weighted magnetization-prepared rapid gradient-echo (MP-RAGE) (2,3). These techniques aim to maximize the intensity difference between WM and GM, and at the same time maintain a high enough signal-to-noise ratio (SNR) to safely distinguish those regions from the suppressed CSF signal. Typically, an image segmentation algorithm (1), which is usually intensity-based, complements this approach.

Even though the three tissue types differ in terms of both proton density and relaxation times, which should result in well-defined distinct intensity values for each category, the segmentation problem is by no means trivial. The tissue classification process is often hampered by issues such as limited contrast-to-noise ratio (CNR), resolution, and partial volume effects. Furthermore, intensity inhomogeneities, even within the same type of tissue, severely hamper tissue separation. A significant part of the spatial variations can be attributed to inherent system limitations, such as radiofrequency (RF) coil inhomogeneities and noise, as well as to normal variation in tissue homogeneity (4,5).

Partial volume effects arise when a voxel is composed of a mixture of different tissue types. Since the signal is a weighted sum of different tissue types, the resulting intensities can fall in between the signals originating from these different tissue values, causing ill-defined edges and dispersion of the expected intensity values. In this case, either multiple images or prior knowledge combined with modeling are needed in order to classify pixels as belonging to one or more tissue categories (6–8).

A further difficulty comes into play in the context of functional mapping in applications such as BOLD fMRI. Functional data are typically acquired using echo-planar imaging (EPI), which is known to be susceptible to geometric distortions due to off-resonance effects. Anatomical images, on the other hand, are normally acquired with multishot acquisitions (e.g., fast low-angle shot (FLASH) or fast spin echo (FSE)), which have relatively little geometric distortion. This introduces a further level of complexity to the coregistration problem.

Imaging of a single-tissue type in the brain by zeroing two tissue types with the use of a double inversion recovery (IR) sequence (9) was originally proposed by Redpath and Smith (10). Double IR is efficient in dealing with partial volume effects because the signal from the unwanted tissue types is suppressed (ideally close to zero), and tissue suppression is not dependent on reception field inhomogeneities, thus bypassing one of the causes of problems in traditional tissue segmentation. However, its efficacy depends on the accuracy of the a priori T_1 estimation and the uniformity of T_1 in the desired tissue types.

In this paper, a new optimized sequence is presented that further elaborates on the concept of zeroing tissue signal based on T_1 relaxation. Our initial motivation was to derive a high-quality GM image that could serve as an anatomical reference for combination with BOLD fMRI data for the purpose of functional mapping. Given practical constraints, in terms of both minimizing subject motion and maximizing the time available for the functional experiment, the technique

Advanced MRI Section, LFMI, NINDS, National Institutes of Health, Bethesda, Maryland, USA.

*Correspondence to: Vasiliki N. Ikonomidou, Advanced MRI Section, LFMI, NINDS, National Institutes of Health, Bldg. 10, Rm. B1D-722, MSC 1065, 9000 Rockville Pike, Bethesda, MD 20892-1065. E-mail: viko@nih.gov

Received 4 November 2004; revised 8 February 2005; accepted 4 March 2005.

DOI 10.1002/mrm.20561
Published online in Wiley InterScience (www.interscience.wiley.com).

was required to provide whole-brain coverage within a measurement time of about 10 min.

A generic pulse scheme was assumed that consisted of a variable number of RF pulses followed by gradient-recalled EPI acquisitions. By appropriately combining the acquired images, one should be able, based on T_1 weighting, to derive three separate images (one for each of the major tissue types). The method should compensate for small errors in initial T_1 estimates with only a minor CNR penalty. Simulated annealing (11,12) was used to determine the number, timing, and flip angles of the RF pulses involved. Noise levels in the resulting single-tissue type images, calculated for a constant reference level of signal, were used as the optimization criterion.

MATERIALS AND METHODS

Sequence Design

T_1 Preparation

T_1-based magnetization preparation can be described as the interaction of two main factors: 1) RF excitation pulses, which drive magnetization away from equilibrium, and 2) longitudinal relaxation, which describes the return of magnetization to the equilibrium position among the axis of B_0. Based on magnetization evolution during this process, the expected signal can be described by a function $b(t)$, as shown in Appendix A.

Tissue differentiation by T_1 contrast is based on the different characteristics of $b(t)$ for each tissue type. Assuming that the MR image is instantaneously obtained at time t_i, the signal contribution from the k-th tissue type will be weighted by the factor $b_k(t_i)$.

Our initial assumption was that brain matter consists mainly of WM, GM, and CSF, which can be approximately represented by a set of average T_1 values $\{T_1^{WM}, T_1^{GM}, T_1^{CSF}\}$. If this description is adequate, the magnetization evolution and therefore the resulting signal of the three tissue types can be estimated by the functions $b_1(t)$, $b_2(t)$, and $b_3(t)$, respectively.

In the acquired data, the signal from each pixel can be regarded as the inner product of the concentration vector for each tissue type $C = [WM,GM,CSF]$ and the vector describing the T_1 weighting for the particular image $B_i = [b_1(t_i),b_2(t_i),b_3(t_i)]$. Assuming that the individual images are linear combinations of the concentration and the weighting vectors formed as $S_i = B_i \cdot C^T$, it is possible to obtain a least-squares estimate of C if at least three images with different T_1 weightings are available:

$$\hat{C} = [(B^T B)^{-1} B^T] S \qquad [1]$$

where S is a vector that contains the differently-weighted image data, and B is a matrix composed of the B_i vectors for all of the acquisitions.

The equation

$$A = [a_{ik}] = (B^T B)^{-1} B^T \qquad [2]$$

describes a matrix of weighting factors that are calculated using numerical estimates of the B matrix based on the selected imaging times t_i and flip angles φ_i, and are subsequently used to add the acquired images.

Equation [1] yields three composite images, each of which shows an estimate of the concentration of one of the tissue types of interest.

Such a scheme is insensitive to inhomogeneities in the MRI reception profile, since these are assumed to affect all acquired images in identical manner. Hence, even though intensity variations caused by these inhomogeneities will still affect the combined images, they will not interfere with the tissue separation process.

Sequence Optimization

The aim of the optimization was to find the number and characteristics of preparation pulses and acquisitions that would result in the largest CNR in the combined images. The parameters to be optimized included the flip angles and timing of a variable number of pulses that were followed by gradient-echo image acquisitions. Gradient-echo rather than spin-echo acquisitions were chosen because of their reduced interference with the magnetization preparation scheme. In the results, pulses with flip angles less than 1° were ignored, as were acquisitions following pulses with flip angles within 1° of 180°. In the latter case, where the pulses were set to 180°.

Since contrast between different tissue types is defined by Eq. [1], maximizing CNR is equivalent to minimizing noise in the combined images. To estimate noise behavior, Gaussian white noise with a probability density distribution $N(0,\sigma^2)$ is assumed for the raw images. The noise is considered to be statistically independent between subsequent image acquisitions. Under these assumptions, the noise in the combined image has the probability density function $N(0,\sum_i a_{ik}^2 \sigma^2)$ and noise power will be multiplied with the factor $\sum_i a_{ik}^2$.

Thus, the main point of the mathematical treatment was to minimize the quantities $\sum_i a_{ik}^2$ while maintaining a constant reference level of signal in the three different types of image combinations, resulting in a maximum SNR in the WM-only, GM-only, and CSF-only images. This can be achieved by varying the functions $b_j(t_i)$, which is equivalent to varying the number of pulses, timing, and flip angles involved in the magnetization preparation and the image acquisition. By starting with a sufficiently large number of RF pulses, and making no assumptions other than the use of gradient-recalled EPI as the acquisition strategy, and a minimum time interval between pulses to allow sufficient time for the acquisition, it is reasonable to assume that the resulting solution is close to a global optimum.

The cost function is a weighted sum of the noise amplification factors for the three segmented images, in the form $\sum_k w_k \sum_i a_{ik}^2$, where w_k represents the relative weighting of the noise factor of the k-th tissue type. Weight selection was an empirical process, reflecting a trade-off in SNR between the GM only image, which proved to be the most difficult to isolate, and the WM and CSF images. The rationale for the trade-off was to minimize the noise power in the GM-only image, while preserving image quality in the other two images. The function was complemented by additional checks for maximum sequence duration (TR) and minimum intrapulse duration, If the checks were failed, they would add a significant penalty to the cost value.

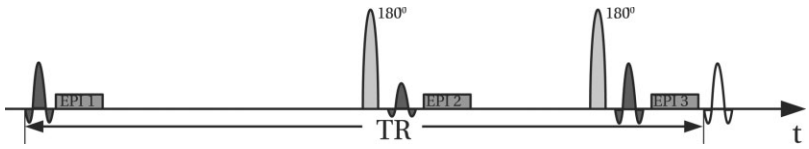

FIG. 1. General scheme of the optimized sequence: three imaging pulses (dark gray) are followed by EPI acquisitions and interleaved by two inversion pulses (light gray). The sequence is repeated with the *z*-encoding stepped every TR.

The complex hyperplane described by the cost function posed a difficult optimization problem that exhibited a large number of local minima. Therefore, the simulated annealing algorithm (11–13) was chosen, which is briefly described in Appendix B.

To estimate the general form of the sequence, the first step was to assume different numbers of pulses (from 9 to 13), for a sequence lasting less than 10 s per TR. The maximum TR was selected based on the measurement time requirements of a high-resolution 3D anatomical brain scan. In each case the optimization converged to a scheme consisting of five pulses (three imaging pulses interleaved by two inversions). The scheme is shown in Fig. 1. We tested the validity of the solution by repeating the optimization procedure several times using different initial estimation values, and different values for the maximum duration allowed per TR.

Even though this optimization is sufficient to yield the full set of parameters for the sequence, for the purpose of calculating, fine-tuning, and testing the parameters and the behavior of the five-pulse sequence, the optimization was rerun while the number of variables was limited to the flip angles of the three imaging pulses and the timing of both imaging and the inversion pulses. This simplification of the optimization problem aided convergence and significantly reduced computation time. Several different sets of T_1 values were tried for the optimization; however, the focus was on three different sets, reflecting literature values for 1.5 and 3.0 T (14,15), as well as our measurements for 3.0 T, using cortical GM and subcortical WM for the T_1 estimates. The constraints imposed on the optimization process were a minimum intrapulse interval of 100 ms, and a maximum TR in the range of 6–10 s. Optimization was carried out again using simulated annealing, with the additional step of a Powell optimization (16) as the last stage, which provided for a relatively fast convergence. The simulated annealing algorithm and optimization process were implemented in IDL (Research Systems Inc.), following the code in Ref. 16. As suggested in Ref. 16, frequent restarts were used to facilitate convergence.

MRI Scanning

The optimum sequence that resulted from the simulations was implemented on a GE 3.0 T whole-body scanner, with a detunable transmit coil and a 16-channel Nova receive-only coil and in-house-built digitizer (17). The preparation scheme was combined with a gradient-recalled EPI acquisition scheme with an additional phase-encoding gradient in the *z*-direction, stepped at each repetition of the five-pulse sequence. Ramp sampling was used to accelerate the acquisition. The EPI readout was followed by a spoiler gradient to dephase any remaining transverse magnetization. Since the acquisitions were sufficiently apart in time to prevent the buildup of stimulated echoes, no additional RF scrambling was employed. The inversion pulses were implemented as adiabatic frequency-offset corrected inversion (FOCI) pulses (18), which provided for independence of the inversion profile from imhomogeneties of the amplitude of the excitation RF field (B_1). Navigator correction was used for zero-order phase correction in order to account for phase errors between *z* phase-encode steps. Three additional repetitions of the five-pulse sequence were added before the start of the acquisition to allow magnetization to reach equilibrium conditions. Both conventional and SENSE (19) gradient-recalled, in-plane, single-shot EPI were used. The image acquisition was preceded by a noise measurement for noise-weighted coil combining, and, in the case of SENSE imaging, by the acquisition of 3D reference volumes for coil sensitivity calibration (20). For the latter, the T_1 preparation scheme was turned off. To ensure image intensity uniformity, a birdcage-type receive coil was simulated by the addition of individual coil images after their phase was normalized to the center of the image (17). The sequence was tested on six healthy volunteers, who were scanned after they gave informed consent under an IRB-approved protocol.

Image Analysis

After the EPI images were reconstructed (17), the first stage of postprocessing involved the calculation of the image combination coefficients. These were derived from Eq. [2], which allows three sets of coefficients (one for each type of image) to be calculated. The explicit aim of the image coefficient calculation was to set in each image the signal from the unwanted tissue types equal to zero. In the realistic situation of the presence of a range of T_1 values, this leads to a T_1-based filtering, as described by the curves shown in Fig. 2.

As detailed below, several subsequent corrections can be made to further optimize image quality and remove imperfections that arise from variations of T_1 values and flip angle, phase drift, and intensity variations.

Compensation for Spatial Variation in T_1

The sequence optimization, as described above, relies on a set of T_1 values to describe the average behavior of the three different tissue types. However, the exact values used in the optimization are not critical. Small variations in T_1, which are normal across different subjects and different parts of the brain, can be compensated for by recalculating the coefficients $b_j(t_i)$ in Eq. [2] for the new T_1 values. The T_1 values can be selected either by visual inspecting the component maps or by calculating the values that minimize the signal in homogeneous regions of interest (ROIs).

To estimate the SNR penalty for the coefficient recalculation, the theoretically expected noise amplification factors for the coefficient recalculation of a sequence opti-

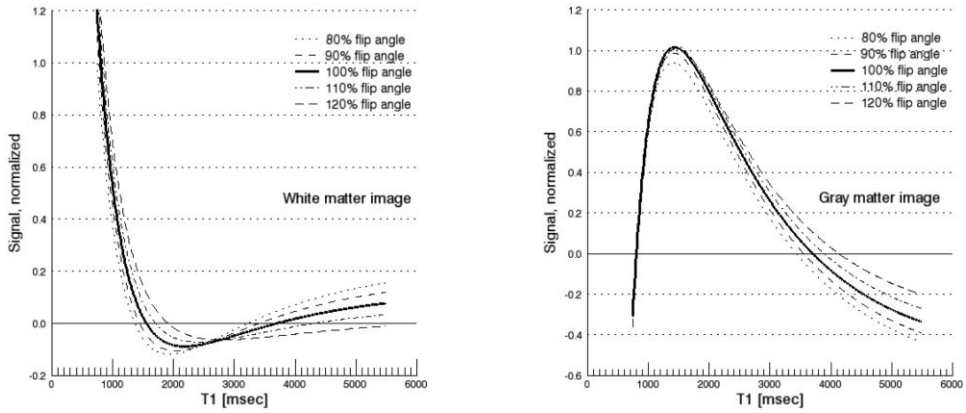

FIG. 2. Simulated signal intensity in the WM- and GM-only images as a function of T_1. Additional dotted lines indicate the effect of flip angle deviation.

mized for T_1 values of 800, 1550, and 3700 ms for WM, GM, and CSF, respectively, were compared with the noise amplification factors of sequences that were explicitly optimized for the actual sets of T_1 values. The ranges of interest were 750–900 ms for WM, 1250–1650 ms for GM, and 3500–4500 ms for CSF. As indicated by the maximal values of relative noise power amplification over those ranges, which are given in Table 1, the noise behavior in the GM image is remarkably stable, while the behavior in the other two images is still acceptable, especially if the actual T_1 values are sufficiently close to the previously estimated ones.

Transmit Profile Compensation

A second type of postprocessing deals with compensating for flip angle variations. Even though the use of adiabatic pulses resulted in accurate inversions, B_1 field inhomogeneities affected the imaging pulses, which resulted in flip angles that were within 80–120% of the target values. As shown in Fig. 2, this results in a deformation of the contrast curve. In the GM image, zeroing of the WM appears to be insensitive to normal flip angle variations; however, there is a problem with the contribution of CSF, which can potentially grow up to 10% of its full signal value. The problem can be exacerbated by the relatively high proton density and T_2^* values of CSF. The same is true for the WM image, even though there the change in T_1 weighting is smaller, and the unwanted CSF signal is kept to less than 5% of its full signal value. Within the normal range of flip angle variation in our scanner, the residual signal resulting from the flip angle deviation was small but noticeable, especially at the edges of the head, and resulted in a rim of CSF around the brain. Therefore, an estimation of the B_1 field based on independent measurements was taken into account for the combination coefficient calculation. It should be noted here that high accuracy is not critical for the flip angle correction, and hence a rough field estimate should be adequate. The CNR loss due to flip angle deviation is shown in Fig. 3, where it can be seen that by correcting the image, it is possible to recover up to 15% of the original CNR.

Phase Drift Compensation

After the combination coefficients were calculated, the raw images were added in their complex (magnitude and phase) form. Phase errors between the images, which can easily arise due to subject motion or hardware drift, posed the first challenge for the image addition scheme. These were overcome by normalizing the image phase. The phase of one image served as reference in order to calculate the phase difference modulo π between the reference and the other two images. The reason we used modulo π instead of the usual modulo 2π was to preserve sign differences due to the inversion process. Furthermore, a shift of the wrapping window, similar to the one described in Ref. 21, was applied to avoid abrupt phase value changes if the phase difference between two images happened to be around $\pi/2$. Subsequently, two fourth-order polynomials were fitted to the differences, and subtracted from the phases of the respective images. Alternatively, for situations with

Table 1
SNR Cost for Coefficient T_1 Recalculation*

	White matter image	Gray matter image	CSF image
White matter (750–900 ms)	17.3% (92.3%)	4.4% (97.9%)	13.4% (93.9%)
Gray matter (1250–1650 ms)	2.5% (98.7%)	0.6% (99.7%)	6% (97.1%)
CSF (3500–4500 ms)	11% (94.9%)	3% (98.5%)	8.8% (95.9%)

*Maximal noise power amplification increase and corresponding relative SNR (in parentheses) resulting from recalculation of the combination coefficients in order to accommodate for T_1 variation. The ranges of T_1 values considered were 750–900 ms for white matter, 1250–1650 ms for gray matter, and 3500–4500 ms for CSF. The sequence was originally optimized for T_1s of 800 ms for white matter, 1550 ms for gray matter, and 3700 ms for CSF. Percentages are given with respect to optimized sequences for the particular T_1 combinations.

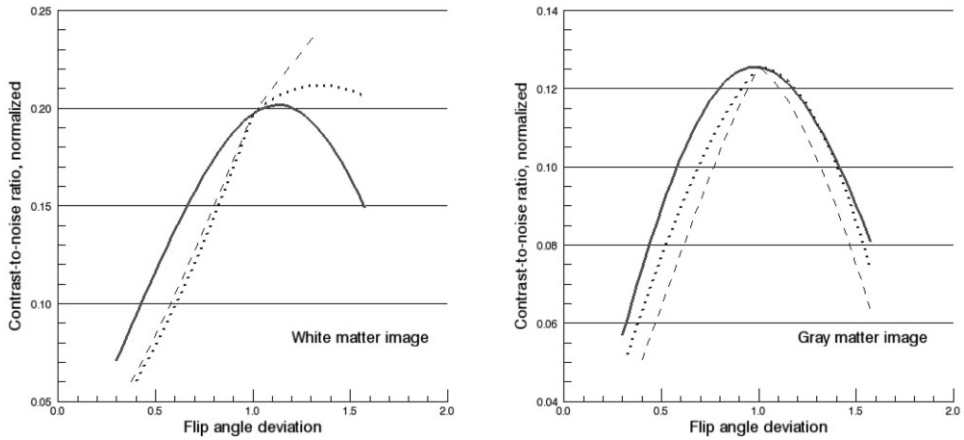

FIG. 3. Effects of flip angle deviation, given as the ratio of the actual over the nominal flip angle, on the CNR of the combined images. In the data for the composite GM image (right), the corrected image (solid line) has higher CNR values than the noncorrected ones for contrast between WM and GM (dotted line), and GM and CSF (dashed line). In the data for the composite WM image (left), the signal in the WM rises more than that in GM or CSF, resulting in higher CNR values between WM and GM (dotted line), and WM and CSF (dashed line) for the noncorrected images compared to the corrected one (solid line). However, if signal suppression is sought, correction should be applied. SNR values are normalized to the values attainable from an EPI acquisition with 90° flip angle.

low SNR, the use of magnitude images when the expected sign of the acquired images was constant for each image over the T_1 range of interest proved to be a reliable solution.

Intensity Correction

Even though intensity variations did not affect the proposed tissue separation process, they were still present in the resulting images. To compensate for that, we investigated the use of homomorphic filtering (22,23). However, homomorphic filtering is associated with both edge enhancement and noise amplification in areas of the image with lower signal. The latter effect is prominent in the resulting GM-only image. To avoid this, the low frequency intensity profile was derived from a low-contrast reference image, which was obtained from a reference scan preceding the acquisition or from the SENSE reference scan, or was calculated from the three raw images. In the latter case, the intensity reference image was calculated as a linear combination of the single-tissue type images, as described by Eq. [3]. A sample reference image derived from the three raw images is shown in Fig. 4.

The intensity profile was calculated by fitting the logarithm of the masked reference image with a fourth-degree polynomial. We chose to use polynomial fitting instead of low-pass filtering (as in the case of classic homomorphic processing) to avoid edge-enhancing effects on the outside of the brain. The acquired images were subsequently divided by the exponential of the fitted profile, resulting in the intensity-corrected images.

In principle, it is also possible to produce images that show all three tissues, and at the same time control the T_1-weighted contribution of each tissue. This is achieved by substituting the weighting factors $[a_{ik}]$ of Eq. [2] by a linear combination

$$A_c = [w_{WM}, w_{GM}, w_{CSF}](B^T B)^{-1} B^T \qquad [3]$$

where the values of the combination vector $[w_{WM}, w_{GM}, W_{CSF}]$ are set to the desired contribution of each tissue type. In this case, however, one should take into account that the final images are also T_2^* and proton density-weighted.

Coregistration with BOLD fMRI Data

To demonstrate the applicability of the proposed methodology for coregistering BOLD fMRI data to anatomical images, a visual activation study was performed. The stimulation paradigm was a 7.5 Hz contrast reversing bull's-eye

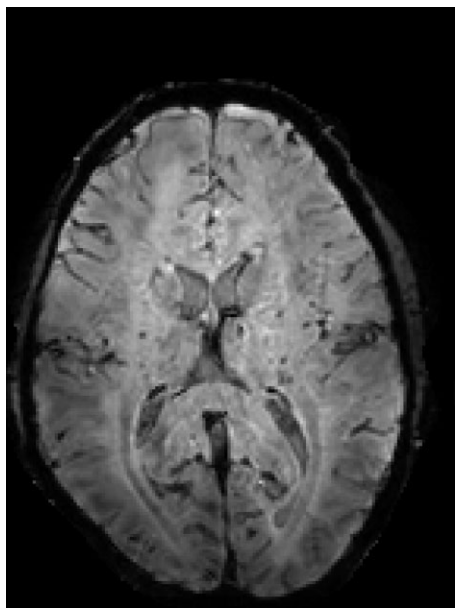

FIG. 4. Intensity reference image, used for intensity correction. The image was created by combining the three raw images acquired with the proposed scheme.

checkerboard that alternated between foveal (central 5°) and peripheral (5–15°) visual fields in a block design manner. The images were shown by back projection on a screen fitted on the Nova receive-only coil. The volunteers could see the screen with the help of a mirror, which was also mounted to the coil. Each block contained 15 scans with a duration of 30 s. Functional data were acquired using 2D gradient-echo EPI with TR = 2000 ms, echo time (TE) = 45 ms, flip angle = 90°, FOV = 220 × 165 mm^2, matrix = 192 × 144, slice thickness/slice gap = 1.8/0.4 mm, and SENSE rate = 2.

For the purpose of coregistration with BOLD fMRI data, anatomical data are acquired using the same in-plane resolution and acquisition characteristics (e.g., EPI readout duration) as the functional scan. This results in the same deformations in both scans, and reduces the registration problem to a rigid-body one.

The first of the EPI acquisitions of the functional scan, which is predominantly T_2^* -weighted, is used as an anatomical reference on which the CSF-only image is registered. This step was deemed necessary to account for slight translation errors between the two scans. After the displacement is calculated, the registration reduces to a simple overlay of the two images.

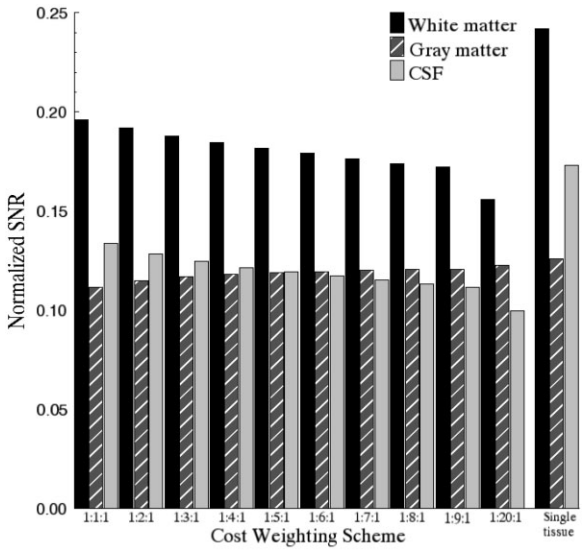

FIG. 5. Expected normalized SNR of the combined images as a function of the cost weighting scheme. TR was kept constant at 6 s per slice. The last set of values refers to three different acquisitions (one for each tissue type).

RESULTS

Sequence Design

The generic form of the optimized sequence consists of three imaging pulses followed by gradient-recalled EPI acquisitions and interleaved with two inversion pulses, as shown in Fig. 1. However, for fine tuning the parameters of the final sequence, there are two issues that should be addressed: the choice of TR and the weights used for the cost function.

The values of the noise amplification factors, and consequently of the cost function, depend on the choice of TR. To limit the overall imaging time, originally TRs below 12 s per slice were considered. In this interval, the noise amplification factors monotonically decrease with TR, with a range of 10–5 for the GM image, 6–3.5 for the WM image, and 11–5.5 for the CSF image. The expected SNR in the combined images can be calculated as the ratio of the SNR of a prototype, non-T_1-weighted 90° flip angle image over the noise amplification factors. The normalized value of SNR divided by the square root of TR, which is often referred to as the "SNR per unit time," can be used as a guide to determine optimal TR. For the T_1 values under consideration, this reached a maximum at about 10.5 s per TR. However, concerns about the overall experiment duration in a 3D high-resolution experiment led us to choose a shorter TR of 6 s per slice. The SNR efficiency trade-off for this duration was an approximately 15% loss of SNR per unit time in the GM-only image, and 10% loss in the WM-only image.

The weights elected for the cost function affect the noise amplification values. By favoring the GM image in the cost function, it is possible to gain up to about 10% in SNR compared to an equally weighted cost function. As shown in Fig. 5, the penalty for this gain is SNR loss in the WM and CSF images. In the extreme case, the cost function is determined only by the SNR of the GM image. Then the optimization process yields the double IR sequence, with the Ernst angle (for GM T_1 and overall TR) as the flip angle of the imaging pulse. It should be noted, however, that this is not the case in the optimization for a single WM image, where the double IR solution results are suboptimal. For the GM image, as shown in Fig. 5, the SNR penalty for acquiring the two additional images is very small. In choosing the weighting scheme, one should take into account that the SNR of the final image depends also on proton density and T_2^* weighting, and that the SNR penalty for the two remaining images when compared to the SNR gain in the GM-only image quickly renders the trade-off inefficient, as shown in Fig. 5. Hence, a weighting of 3:18:2 for the WM, GM, and CSF images, respectively, was chosen.

After the TR and the cost weighting scheme were selected, the sequence parameters for different sets of T_1's, corresponding to both literature values and our own T_1 measurements, were calculated. The time required for a single optimization was about 4 min on a dual AMD MP 2600+ based personal computer. Sample parameter sets are given in Table 2.

Three sample images corresponding to the three acquisitions are shown in Fig. 6a–c. Their different T_1 weightings allowed the WM, GM, and CSF images shown in Fig. 6d–f to be derived by means of linear combination.

With a TR of 6 s, whole-brain coverage at 1.15^3 mm^3 isotropic resolution (matrix = 192 × 144 × 96, FOV = 220 × 165 × 110 mm^3) was achieved in 10 min 21 s. A SENSE rate of 2 was used in the second dimension to reduce T_2^* blurring and geometric distortions. Sample images are given in Fig. 7. For 1.7^3 mm^3 isotropic resolution over the same volume (matrix size = 128 × 96 × 64), corresponding to a typical fMRI study, the scan duration is 6 min 42 s.

Table 2
Sequence Parameters*

T_1(ms) WM; GM; CSF	Imaging pulse #1	Inversion pulse #1	Imaging pulse #2	Inversion pulse #2	Imaging pulse #3
800; 1550; 3700	0 ms / 46°	3020 ms	3573 ms / 23°	5112 ms	5575 ms / 83°
832; 1331; 3700	0 ms / 65°	315 ms	3685 ms / 23°	5243 ms	5695 ms / 77°
700; 1050; 3500	0 ms / 76°	3362 ms	3809 ms / 24°	5346 ms	5724 ms / 73°

*Examples of optimized scheme parameters for different sets of T_1s (given in ms in the first column). The first row corresponds to our T_1 measurements, the second row to values given for 3 T by Wansapura et al (16), and the third for estimated values at 1.5 T based on values from Breger et al (15). TR was kept at 6 s, and the cost weighting scheme was 3 for the white matter, 18 for the gray matter, and 2 for the CSF image.

Image Contrast

The combination of a maximized signal difference with an optimized SNR behavior leads to an optimized CNR behavior. Table 3 shows average SNR values for images with 1.15 mm isotropic resolution (96 slices), measured over ROIs in the selected structures. As can be easily deduced from the presented values, the ratio of cortical GM signal to WM signal is about 9:1 in the GM image, and 1:9 in the WM image.

However, SNR is affected by a variety of factors, including coil sensitivity, proton density, and the actual T_1 and T_2^* values of the imaged tissues. This results in a significant spread in the measured SNR values, which are reflected in the histograms shown in Fig. 8. To generate these histograms, masks of "pure" GM, WM, and CSF were selected for a typical volunteer by comparing the pixel intensity values in the respective single-tissue type images. The selection was limited to the 37 central slices to avoid regions with signal drop-off due to the slice-selection profile or shimming problems. Thresholds were adjusted to include a large region, while at the same time partial volume effects were minimized. Since the histograms are calculated based on the magnitude images, the SNR distributions follow Rician-like curves, which are particularly evident for the suppressed tissue types.

In general, the lower proton density and T_2^* of WM result in contrast values in the WM image that are comparable to or lower than those of the GM image, while the higher proton density and T_2^* of CSF lead to CNR values above 70 in the CSF-only image. Imperfect tissue suppression due to T_1 variation of physiological tissue is also reflected in the given results. Furthermore, inhomogeneities in the coil sensitivity profile also affect the measured values, with cortical GM showing the highest CNR values because of its proximity to the receive coils.

Figure 8c and d show SNR values normalized to the SNR values of a nonweighted EPI image of the same resolution and SENSE rate, obtained using a 30° nominal flip angle, 48-ms TE, and 140-ms TR. The objective of this comparison was to minimize the effects of receiver sensitivity to the final SNR distribution. Variations in T_1, flip angle, and phase errors still cause a significant widening in the distributions; however, the peaks are clearly distinguishable.

As a further evaluation, the proposed method was compared with a manufacturer-provided MP-RAGE sequence (inversion time (TI) = 725 ms, delay time (TD) = 1400 ms,

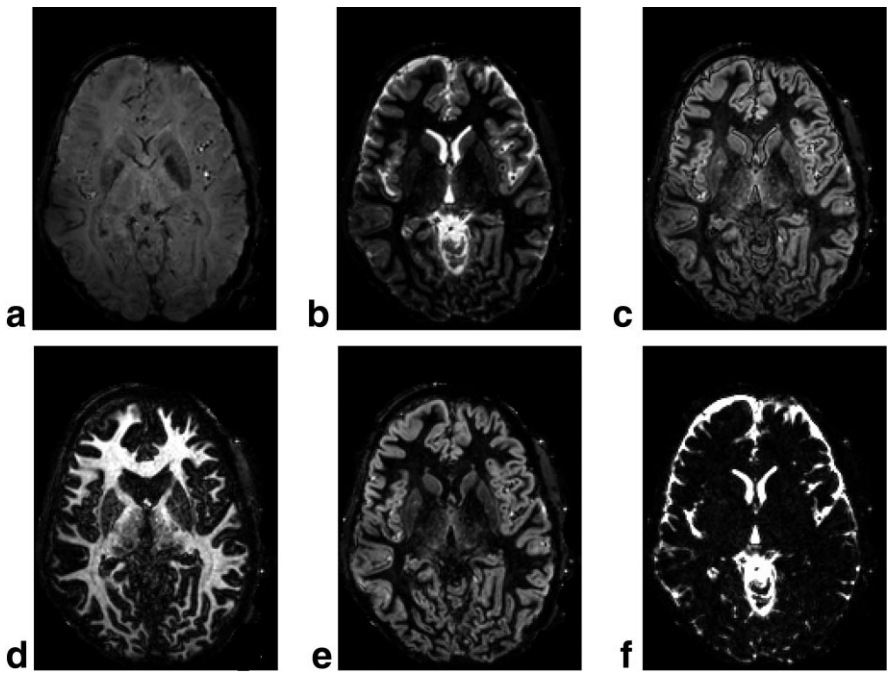

FIG. 6. Raw images (**a–c**) acquired with the proposed sequence. Their weighted combination yields the single-tissue type images shown in **d–f**. Skull tissue signals are still visible in d and e.

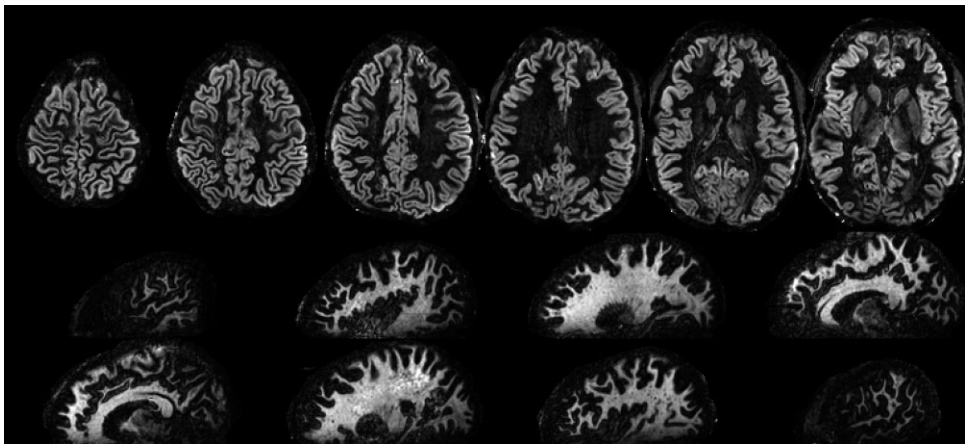

FIG. 7. Axial oblique GM images and sagittal oblique WM images obtained during a 3D scan with the proposed method. Coverage of a 220 × 165 × 110 mm^3 FOV with a 192 × 144 × 96 matrix was achieved in 10 min 21 s.

flip angle = 6°, TR = 5.7 ms, readout time (TACQ) = 2.048 ms). Simulated SNR values for the proposed EPI sequence and the MP-RAGE sequence are given in Table 4. The results show that for resolutions attainable without SENSE, the CNR values (per unit scan time) obtained with the proposed method are comparable to those obtained by an MP-RAGE sequence of the same nominal resolution. An experimental comparison on a single volunteer using a standard GE birdcage head coil and no *k*-space apodization during image reconstruction yielded CNR values of about 9.8 for the WM image, 8.3 for the GM image, and 5.1 for the MP-RAGE image, as measured between homogenous regions of frontal WM and GM in the caudate nucleus. Normalized by the square root of TR in seconds, this yields a CNR/unit time of 0.49 for the WM image, 0.41 for the GM image, and 0.33 for the MP-RAGE image.

Coregistration with BOLD fMRI Data

Figure 9 displays the overlay of BOLD fMRI data (*t*-score maps) from a foveal and peripheral visual field stimulation experiment onto GM anatomical maps resulting from the proposed sequence. The use of EPI with the same readout train ensures that the images have the same geometric distortions, and thus removes one of the main uncertainty factors in the registration problem. The only correction process necessary is a rigid-body registration to account for small displacements between the scans. Hence, in the final overlay images, it is easy to see the excellent spatial correlation of the activation patterns with the underlying anatomy.

Table 3
Signal-to-Noise Ratio Measurements*

	Gray matter image	White matter image
Cortical gray matter	55	5
White matter	6.5	46.5
Caudate nucleus	27.5	6.5
Putamen	21	11
Thalamus	22	13
CSF	7.5	4

*Average signal-to-noise ratio estimates over different parts of the resulting images. Measurements were taken from 3D EPI acquisitions with matrix size 192×144×96 covering a 220×165×110 mm^3 FOV with SENSE rate 2 (six normal volunteers). The values were measured in homogeneous regions of interest, in different regions of the brain and away from obvious artifacts.

DISCUSSION

Sequence Design

The new imaging sequence presented in this work is the solution of an optimization problem. To address this problem, we developed a T_1-based magnetization preparation and image acquisition strategy whereby the addition of acquired images would result in three single-tissue type images showing WM, GM, and CSF, with maximal SNR values. The constraints of the problem, which correspond to the initial assumptions, are the maximum TR, the minimum time interval between subsequent RF pulses, and the use of gradient-recalled EPI for image data acquisition. The double IR scheme and the three variable flip angle image acquisitions emerged as a result of the simulated annealing process.

Furthermore, the presented mathematical treatment demonstrates that an appropriate formulation of the cost function combined with a versatile optimization algorithm can be applied to the generic problem of magnetization preparation at the level of sequence design, and not just for value optimization. Simulated annealing offered the necessary robustness to deal with a complex optimization problem. The emergence of the double IR scheme verified that double IR is the optimum solution for the problem of nullifying two tissue types based on T_1 contrast. In addition, the reduction of the free variables at the second stage of the optimization allowed the parameters to be calculated in in a reasonable time, and provided an easy way to adjust the sequence to different T_1 values and to try a variety of cost functions with different weighting schemes.

The main advantage of the proposed method over the double IR technique proposed by Redpath and Smith (10) is that it does not require a precise estimate of the tissue T_1's before the data are acquired. A reasonable variation of T_1 values, which is normally expected both between different subjects and within different areas of the same brain, can be taken into account during the postprocessing stage, by appropriate recalculation of the combination coefficients. Therefore, the proposed method appears to be

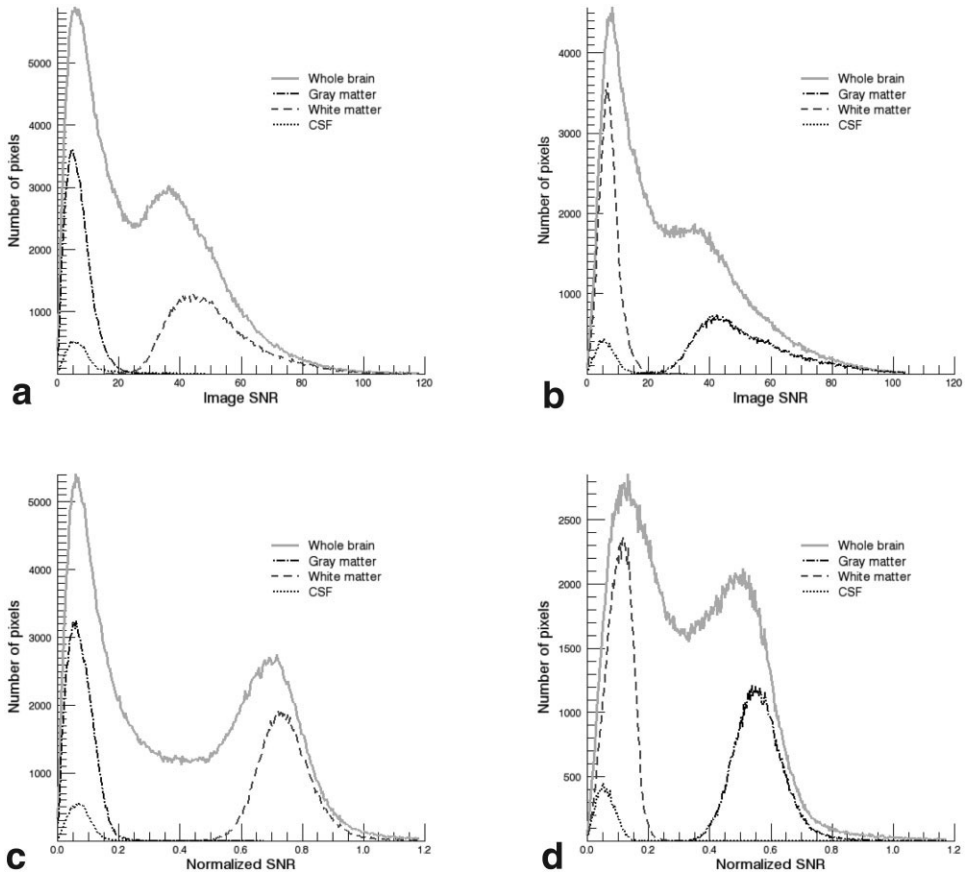

FIG. 8. SNR histograms from images of a normal volunteer. Graphs **a** and **b** show SNR distributions for the three tissue types and the whole brain of the noncorrected GM and white images, respectively. In graphs **c** and **d**, the values have been normalized to the SNR values of a nonweighted EPI reference image. Data are based on the 37 center slices of a 96-slice set.

more suited for routine use. Furthermore, it allows the simultaneous acquisition of GM, WM, and CSF images, as opposed to the single-tissue type image offered by the double IR method in the same amount of time.

In the work presented here, EPI was chosen because it is the work horse for BOLD fMRI studies, and because it offers high efficiency in terms of SNR and image encoding speed. An important drawback of EPI is its sensitivity to geometric distortions and T_2^* blurring, which ultimately limit the achievable image resolution. Although EPI artifacts can to some extent be corrected, they must be taken into account when evaluating the images. Potentially, one could reduce EPI-related artifacts by either increasing the SENSE rate or using interleaved EPI schemes, at the cost of scan time and motion sensitivity. Special care must be taken regarding the EPI fat ghosting. Because fat has a low T_1 value, the presented adding scheme can significantly enhance such ghosting, as can be derived by extrapolating the curves in Fig. 2 for the T_1 values corresponding to fat. Appropriate fat suppression is critical for the quality of the final images.

Flip angle dependence, a well known problem in T_1 measurement methods, is present but is not critical. If qualitative results are sought, the high CNRs provided by

Table 4
Expected SNR Values: Simulation Results*

T_1 (in ms)	EPI-GM image	EPI-WM image	MP-RAGE
800–840 (WM)	0.0–4.9	38.6–43.7	56.4–59.9
1300–1600 (GM)	33.7–34.7	0.0–7.4	21.5–33.4
3700–4300 (CSF)	0.0–7.8	0.0–2.5	2.5–6.1

*Simulated SNR values (normalized per unit time-arbitrary units) for two different acquisitions of a 128×96×64 matrix. The EPI scheme is based on the first preparation scheme of Table 1 and combined for T_1 values of 800 ms, 1550 ms, and 4000 ms for white matter, gray matter, and CSF respectively. EPI characteristics: TE = 48 ms, 557 μs per echo and 6 min 41 sec total acquisition time. MP-RAGE simulation was based on a manufacturer provided implementation, with TI = 725 ms, TD = 1400 ms, 6° flip angle, sampling rate 16 μs per sample, TR = 5.7 ms, and TE = 2 ms. Average tissue water density was assumed as $\rho = 0.708$ for white matter, $\rho = 0.832$ for gray matter, and $\rho = 1$ for CSF (24), while average T_2^* was assumed at 48.9 ms (25) for gray and white matter, and it was not taken into account for CSF.

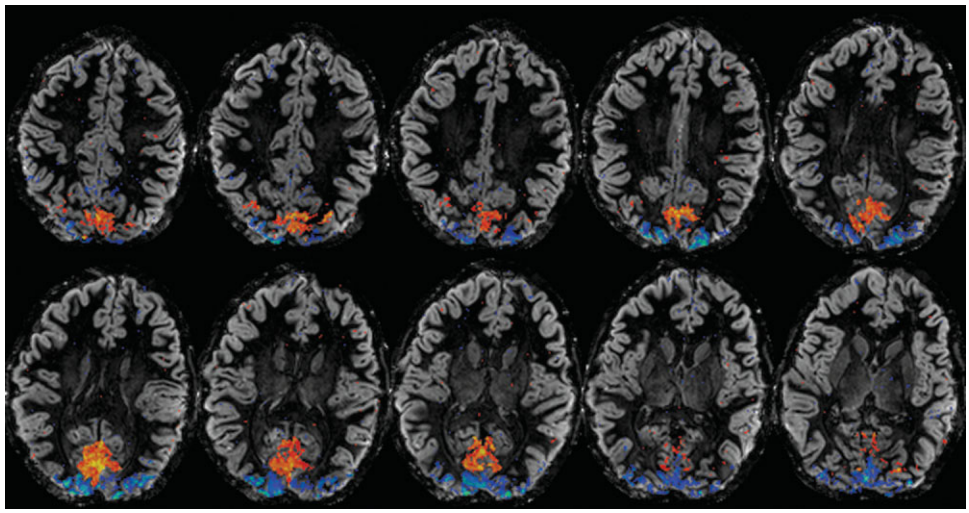

FIG. 9. Overlay of fMRI data on anatomical GM maps. The functional data (*t*-score maps) corresponding to foveal and periphery visual field stimulation paradigms were acquired using 2D gradient-echo EPI with TR = 2000 ms, TE = 45 ms, flip angle = 90°, FOV = 220 × 165 mm^2, matrix = 192 × 144, slice thickness/slice gap = 1.8/0.4 mm, SENSE rate = 2. The anatomical data were obtained using 3D, in-plane, single-shot, gradient-echo EPI with TE = 48 ms, matrix = 192 × 144 × 96, FOV = 220 × 165 × 110 mm^3, SENSE rate = 2. Since both the anatomical and functional data were acquired using in-plane, single-shot EPI acquisitions with the same parameters, they exhibit the same deformations, which facilitates the coregistration.

the proposed method can compensate for the deviations caused by a normal range of flip angle variation. If quantitative results are desired, the effects of flip angle deviation can be corrected by using a B_1 map to calculate the combination coefficients.

On the other hand, inhomogeneities of the reception profile have no effect on the tissue separation process. Even though intensity inhomogeneities are present in the final images, the separation process depends only on the relationship between the signal in the three acquisitions. Since the combination process is linear, a multiplicative factor (e.g., coil sensitivity) does not affect it, and it is transferred, unchanged, to the final images, where it can be corrected using image-processing techniques like the one presented.

Image Contrast

The results of both the theoretical evaluation and the in vivo experiments show that the proposed method is capable of providing high-contrast anatomical images, with CNR comparable to that achieved by established techniques.

From the experimental results, it follows that the combination of the proposed sequence with the 16-channel Nova head coil can yield GM images showing an average CNR on the order of 40–50 between cortical GM and WM, at an isotropic resolution of 1.15^3 mm^3 in less than 11 min. The slightly lower values in the WM image are due mainly to the coil sensitivity profile, the greater dependence of the WM image on the accuracy of the initial T_1 estimation, and the lower proton density of WM, which result in overall smaller CNR values.

As with any sequence that produces T_1-weighted images, the contrast values depend on the actual T_1 values of the tissues involved. This means that contrast is affected by T_1 variations both within different regions of the brain of the same subject and between different subjects (14,15,26–28). The steep slope of the T_1 response curve (Fig. 2) around the zero point shows that the method is sensitive to even small variations of T_1 for the first zeroed tissue (WM in the GM image, and GM in the WM image). Recalculating the image combination coefficients for slightly different T_1's can help accommodate T_1 variations.

The initial assumption of the method—that the received signal is the linear sum of signals originating from different tissue types—takes into account partial volume effects. Because of the linearity of the method, the image combination should be as effective in suppressing the signal from the unwanted tissue types whether there are signals from other tissue types in the same voxel or not. Hence, the ratios formed in Table 3 (ranging from 1:9 to 1:3) are indicative of the suppression of partial volume errors in the resulting images.

When compared with state-of-the-art anatomical techniques, such as the MP-RAGE sequence shown in Table 4, the proposed EPI scheme produces comparable CNR values at lower resolutions with full-FOV acquisitions, especially between the basal ganglia and WM. However, if a representation of cortical GM is sought, as was the initial motivation for this work, there are three additional points that should be taken into account. The first one is that the expected SNR per unit time in the cortical GM is comparable to or higher than that attainable with the MP-RAGE sequence under consideration. Second, the signal values in the GM-only image yielded by the proposed method are almost constant over a wide range of T_1 values, covering the normal range of variation of GM T_1. In contrast, over the same range of T_1 values the expected intensity in the MP-RAGE image varies within 30% of the highest expected value. The third point concerns the signal ratios in

the resulting images. While both the expected and the measured GM:WM ratio in the MP-RAGE images point toward 1:3, in the EPI images an average signal ratio of 9:1 for cortical GM:WM is measured. This, and the fact that there are three images, each of which provides information about a specific tissue type, make the method more efficient in dealing with the problem of partial volume effects.

Coregistration with BOLD fMRI Data

The proposed method is highly suitable for coregistration with EPI-based fMRI data, since the deformations due to off-resonance effects in both scans can be matched. Because the proposed method uses an EPI acquisition scheme, one can choose identical acquisition characteristics (e.g., resolution, gradient strength, and duration) for both the functional and the anatomical scan. In this case, both scans exhibit the same deformations and can be aligned by rigid-body registration procedures. This should facilitate fMRI interpretation on a case-by-case basis, particularly for high-resolution scans (29,30); however, it will not necessarily simplify the analysis of group data.

CONCLUSIONS

A novel pulse sequence has been presented that is capable of simultaneously producing GM-only, WM-only, and CSF-only images based on T_1 contrast. The proposed method uses an initial estimate of the T_1 values of the tissues involved, but it can use postprocessing to take their variations into account at the cost of a very minor CNR penalty. This increased flexibility compared to conventional methods enables its use in a wide range of subjects.

The proposed pulse sequence, which resulted from an optimization procedure with no prior assumptions as to the generic sequence form, converged to a variant of the double IR technique that is currently used for brain tissue segmentation, and approaches the optimal solution of the tissue separation problem based on T_1 values.

The proposed method is particularly well suited for functional mapping applications because it provides high-contrast anatomical maps using the same EPI acquisition characteristics as the fMRI experiment. Other potential applications may include cortical-thickness measurement or substructure segmentation.

APPENDIX A

If the pulse sequence parameters are known, the function $b(t)$ can be derived from the Bloch equations. By solving for M_z in the absence of an RF field B_1, one gets

$$M_z(t) = M_0 + (M_z(t_0) - M_0)e^{-(t-t_0)/T_1} \qquad [A.1]$$

The effect of RF pulses can be easily modeled as

$$M_z^+ = M_z^- \cos(\phi_j) \qquad [A.2]$$

where φ_j is the flip angle of the jth pulse, and M_z^-, M_z^+ is the longitudinal component of the magnetization before and after the application of the RF pulse, respectively.

Starting at time 0 with initial conditions $M_z = M_z^{in}$, and normalizing by setting $M_0 = 1$, it can be shown that in the generic case of a T_1 preparation consisting of N pulses with flip angles φ_i at time points t_i, $i = 1, 2, \ldots N$, M_z after the N^{th} pulse is given by:

$$M_z(t) = 1 + \left\{ \sum_{i=1}^{N-1} \left[(\cos(\varphi_i) - 1) \left(\prod_{j=i+1}^{N} \cos(\varphi_j) \right) e^{t_i/T_1} \right] + (\cos(\varphi_N) - 1)e^{t_N/T_1} + (M_z^{in} - 1) \prod_{i=1}^{N} \cos(\varphi_i) \right\} e^{-t/T_1}, \quad t > t_N \qquad [A.3]$$

If the sequence is repeated continuously without a system relaxation interval, the equilibrium values for M_z at the end of the preparation scheme, representing the condition $M_z(t_n) = M_z^{in} = M_z^{eq}$ for the equilibrium state, will be:

$$M_z^{eq} = \frac{\cos(\phi_N) + e^{-t_N/T_1} \left\{ \sum_{i=1}^{N-1} \left[(\cos(\phi_i) - 1) \left(\prod_{j=i+1}^{N} \cos(\phi_j) \right) e^{t_i/T_1} \right] - \prod_{i=1}^{N} \cos(\phi_i) \right\}}{1 - e^{-t_N/T_1} \prod_{i=1}^{N} \cos(\phi_i)} \qquad [A.4]$$

It is straightforward to derive the signal weighting factor at the n-th pulse $b(t)$ analytically by substituting $M_z^{in} = M_z^{eq}$ in Eq. [A.3] as

$$b(t_n) = \sin(\varphi_n) \left\{ 1 + \left\{ \sum_{i=1}^{n-2} \left[(\cos(\varphi_i) - 1) \left(\prod_{j=i+1}^{n-1} \cos(\varphi_j) \right) e^{t_i/T_1} \right] + (\cos(\varphi_{n-1}) - 1)e^{t_{n-1}/T_1} + (M_z^{eq} - 1) \prod_{i=1}^{n-1} \cos(\varphi_i) \right\} e^{-t_n/T_1} \right\} \qquad [A.5]$$

The use of n reflects the adjustment of the sum and product limits to the number of points applied up to the desired time point. However, from a programming perspective, especially with sequences that involve many RF pulses, it is easier to calculate M_z^{eq} as a starting value and subsequently numerically evaluate $b(t)$ using Eqs. [A.1] and [A.2].

APPENDIX B

Simulated annealing was originally proposed by Kirkpatrick et al. (12). It is based on an analogy between the

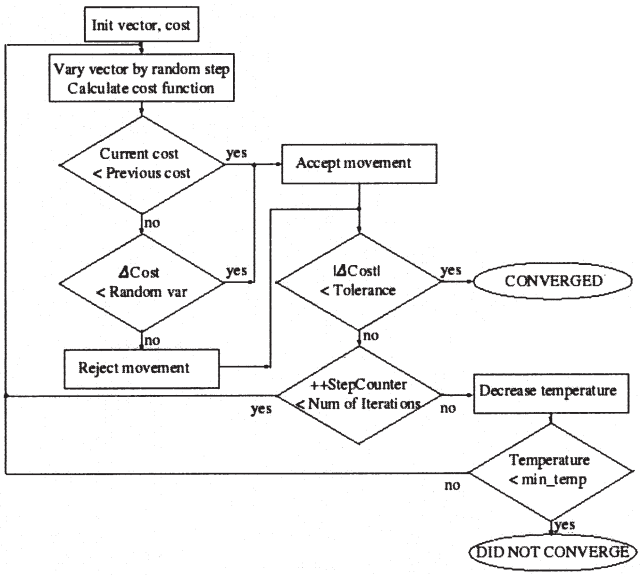

FIG. 10. Flowchart of a basic simulated annealing implementation.

optimization problem and the thermodynamic process of slow cooling-down in molten metals. Due to the thermal energy of the system, atom movements that result in a higher potential energy configuration can occur. By slowly lowering the temperature, and thereby decreasing the thermal energy, the system settles down in a minimum energy configuration.

Simulated annealing imitates this process by allocating an initial amount of "thermal" energy to the system. As shown in Fig. 10, an initial set of values is assumed for the parameters of the optimization. These are varied by random steps. As in any gradient descent method, steps that decrease the value of the cost function are always accepted. However, steps that increase the value of the cost function can also be accepted. In this case, the increase of the cost function is compared to the value of a random variable having a probability density function of the form

$$p = \exp[-\Delta E/T] \qquad [B.1]$$

where T is the assigned system temperature. If the increase of the cost function is smaller than the current value of the random variable, the step is accepted. This helps the system escape from local minima.

The system temperature is decreased during the optimization process. The rules that specify after how many steps and by how much it is brought down are called the annealing schedule. As the temperature drops, the probability of a movement uphill along the energy gradient is reduced, and the optimization process tends to become a conventional gradient descent method. However, if the annealing process is slow enough (i.e., with the appropriate choice of initial temperature and annealing schedule), it can be successful in avoiding local minima.

Vanderbilt and Louie (13) described the application of simulated annealing to continuous variable problems, such as in the present design problem. It has been applied to various MR studies, as parameter estimation for in vivo MR spectroscopy (MRS) (31), or 2D selective excitation pulse design (32). In addition, Epstein et al. (33) applied simulated annealing to MRI sequence optimization.

For the purposes of the sequence optimization described, several initial vectors were tried to ensure convergence stability. Equally distributed times among the selected maximum TR or a known optimal solution for a smaller TR were used, even though the latter may introduce a bias to the results. The sequence vector was varied using random steps, the size of which was controlled by an initial simplex size (16) of 100 ms for the timing variables and 1.0 radians for the flip angles. Based on the vector, the quantities $b_j(t_i)$ were evaluated numerically using estimates of the T_1 values of the tissues of interest. The weights a_{ik} were calculated from Eq. [2]. They were then used to calculate the value of the cost function. Downhill movements were always accepted, and a logarithmically distributed random variable controlled the acceptance of uphill movements, as described in Ref. 16. Although the exact parameters for the simulated annealing optimization depended on both the maximum TR and the T_1 values elected, and were the result of an empirical, trial-and-error process, an initial temperature T of 10^6 with 5000 iterations per annealing cycle resulted in a relatively stable behavior in most cases. Reducing the number of free variables by considering three imaging and two inversion pulses allowed us to reduce the initial temperature to 10^5, and to use 2000 iterations per cycle. This significantly reduced the computing time requirements. At the end of each cycle, T was reduced to $0.98T$.

REFERENCES

1. Clarke LP, Velthuizen RP, Camacho MA, Heine JJ, Vaidyanathan M, Hall LO, Thatcher RW, Silbiger ML. MRI segmentation: methods and applications. Magn Reson Imaging 1995;13:343–368.
2. Mugler JP III, Brookeman JR. Three-dimensional magnetization-prepared rapid gradient-echo imaging (3D MP RAGE). Magn Reson Imaging 1990;15:152–157.
3. Deichmann R, Good CD, Josephs O, Ashburner J, Turner R. Optimization of 3-D MP-RAGE sequences for structural brain imaging. Neuroimage 2000;12:112–127.
4. Guillemaud R, Brady M. Estimating the bias field of MR images. IEEE Trans Med Imaging 1997;16:238–251.
5. Arnold JB, Liow J-S, Schaper KA, Stern JJ, Sled JG, Shattuck DW, Worth AJ, Cohen MS, Leahy RM, Mazziotta JC, Rottenberg DA. Qualitative and quantitative evaluation of six algorithms for correcting intensity nonuniformity effects. Neuroimage 2001;13:931–943.
6. Rajapakse JC, Giedd JN, Rapoport JL. Statistical approach to segmentation of single-channel cerebral MR images. IEEE Trans Med Imaging 1997;16:176–186.
7. Santago P, Gage D. Quantification of MR brain images by mixture density and partial volume modeling. IEEE Trans Med Imaging 1993; 12:566–574.
8. Choi HS, Haynor DR, Kim Y. Partial volume tissue classification of multichannel magnetic resonance images—a mixel model. IEEE Trans Med Imaging 1991;10:395–407.
9. Bydder GM, Young IR. MR imaging: clinical use of the inversion recovery sequence. J Comput Assist Tomogr 1985;9:659–675.
10. Redpath TW, Smith FW. Technical note: use of a double inversion recovery pulse sequence to image selectively grey or white brain matter. Br J Radiol 1994;67:1258–1263.
11. Metropolis N, Rosenbluth AW, Rosenbluth MN, Teller AH, Teller E. Equation of state calculations by fast computing machines. J Chem Phys 1953;31:1087–1092.
12. Kirkpatrick S, Gelatt CD, Vecchi MP. Optimization by simulated annealing. Science 1983;220:671–680.

13. Vanderbilt D, Louie SG. A Monte Carlo simulated annealing approach to optimization over continuous variables. J Comput Phys 1984;56: 259–271.
14. Breger RK, Rimm AA, Fischer ME, Papke RA, Haughton VM. T1 and T2 measurements on a 1.5-T commercial MR imager. Radiology 1989;171: 273–276.
15. Wansapura JP, Holland SK, Dunn RS, Ball WS. NMR relaxation times in the human brain at 3.0 tesla. J Magn Reson Imaging 1999;9:531–538.
16. Press WH, Teukolsky SA, Vetterling WT, Flannery BP. Numerical recipes in C: the art of scientific computing. 2nd ed. Cambridge: Cambridge University Press; 1992.
17. de Zwart JA, Ledden PJ, van Gelderen P, Bodurka J, Chu R, Duyn JH. Signal-to-noise ratio and parallel imaging performance of a 16-channel receive-only brain coil array at 3.0 tesla. Magn Reson Med 2004;51:22–26.
18. Ordidge RJ, Wylezinska M, Hugg JW, Butterworth E, Franconi F. Frequency offset corrected inversion (FOCI) pulses for use in localized spectroscopy. Magn Reson Med 1996;36:562–566.
19. Pruessmann KP, Weiger M, Scheidegger MB, Boesiger P. SENSE: sensitivity encoding for fast MRI. Magn Reson Med 1999;42:952–962.
20. de Zwart JA, Ledden PJ, Kellman P, van Gelderen P, Duyn JH. Design of a SENSE-optimized high-sensitivity MRI receive coil for brain imaging. Magn Reson Med 2002;47:1218–1227.
21. Strand J, Taxt T, Jain AK. Two-dimensional phase unwrapping using a block least-squares method. IEEE Trans Image Processing 1999;8:375–386.
22. Oppenheim AV, Schafer RW, Stockham Jr TG. Nonlinear filtering of multiplied and convolved signals. Proc IEEE 1968;56:1264–1291.
23. Lim JS. Two-dimensional signal and image processing. Englewood Cliffs, NJ: Prentice Hall PTR; 1990.
24. Whittall KP, MacKay AL, Graeb DA, Nugent RA, Li DKB, Paty DW. *In vivo* measurement of T_2 distributions and water contents in normal human brain. Magn Reson Med 1997;37:34–43.
25. Fera F, Yongbi MN, van Gelderen P, Frank JA, Mattay VS, Duyn JH. EPI-BOLD fMRI of human motor cortex at 1.5 T and 3.0 T: sensitivity dependance on echo time and acquisition bandwidth. J Magn Reson Imaging 2004;19:19–26.
26. Kim S-G, Hu X, Uğurbil K. Accurate T1 determination from inversion recovery images: application to human brain at 4 tesla. Magn Reson Med 1994;31:445–449.
27. Jezzard P, Dueweel S, Balaban RS. MR relaxation times in human brain: measurement at 4 T. Radiology 1996;199:773–779.
28. Harvey I, Tofts PS, Morris JK, Wicks DAG, Ron MA. Sources of T1 variance in normal human white matter. Magn Reson Imaging 1991;9:53–59.
29. Cheng K, Waggoner RA, Tanaka K. Human ocular dominance columns as revealed by high-field functional magnetic resonance imaging. Neuron 2001;32:359–374.
30. Beauchamp MS, Argall BD, Bodurka J, Duyn JH, Martin A. Unravelling multisensory integration: patchy organization within human STS multisensory cortex. Nat Neurosci 2004;7:1190–1192.
31. Sekihara K, Ohyama N. Parameter estimation for in vivo magnetic resonance spectroscopy (MRS) using simulated annealing. Magn Reson Med 1990;13:332–339.
32. Hardy CJ, Bottomley PA, O'Donnell M, Roemer P. Optimization of two-dimensional spatially selective NMR pulses by simulated annealing. J Magn Reson 1988;77:233–250.
33. Epstein FH, Mugler III JP, Brookeman JR. Optimization of parameter values for complex pulse sequences by simulated annealing: application to 3D MP-RAGE imaging of the brain. Magn Reson Med 1994;31: 164–177.